Intersubband Electroluminescence from Silicon-Based Quantum Cascade Structures

G. Dehlinger,[1]*† L. Diehl,[1]*† U. Gennser,[1]‡ H. Sigg,[1] J. Faist,[2] K. Ensslin,[3] D. Grützmacher,[1] E. Müller[1]

The quantum cascade laser, which uses electronic transitions within a single band of a semiconductor, constitutes a possible way to integrate active optical components into silicon-based technology. This concept necessitates a transition with a narrow linewidth and an upper state with a sufficiently long lifetime. We report the observation of intersubband electroluminescence from a p-type silicon/silicon-germanium quantum cascade structure, centered at 130 millielectron volts with a width of 22 millielectron volts, with the expected polarization, and discernible up to 180 kelvin. The nonradiative lifetime is found to depend strongly on the design of the quantum well structure, and is shown to reach values comparable to that of an equivalent GaInAs/AlInAs laser structure.

A semiconductor laser typically relies on conduction band electrons and valence band holes being injected through a forward-biased p-n junction into a common region in space, where the probability for a radiative recombination across the band gap is high. The active layer usually consists of a quantum well that is realized using heteroepitaxy of III-V material systems such as InGaAs/InP. A long-standing wish for microelectronics technology has been the integration of semiconductor lasers onto a silicon chip. Silicon-germanium alloys have brought many of the advantages of heterostructures into the domain of the dominating Si technology, but the indirect band gap of the group IV materials is a hindrance to Si-based active optical components. This implies that radiative transitions across the band gap must be accompanied by a large momentum transfer, and are therefore unlikely. Moreover, Si and $Si_{1-x}Ge_x$ alloys usually form heterostructures with staggered band offsets, in such a way that the electrons and holes are spatially separated. These problems are circumvented in the unipolar quantum cascade laser (QC laser) (*1*), where transitions between quantum well levels within a band (so-called intersubband transitions) are used to obtain laser light in the mid- to far-infrared wavelength region. Carriers stream down a potential staircase of coupled quantum wells, passing a sequence of active layers, where the lifetimes of two levels are carefully tuned through control of the tunneling probability and phonon interaction strength in order to obtain population inversion (*1*). The transitions occur without momentum transfer (*2*). Because a single band is used, the nature of the band gap is irrelevant for this type of device.

The QC concept thus may offer a path toward the realization of a Si-based laser device. Furthermore, in comparison to the existing QC systems realized with polar III-V materials (*3–5*), it has been suggested that this system, with a weaker carrier-phonon coupling, may prove advantageous in the long-wavelength region, ≥18 μm (*6*). However, there are important obstacles to overcome, such as (i) the need to accommodate the large built-in strain (there is a 4% mismatch between the Si and Ge lattices), (ii) the need to work in the physically more complex valence band (coupled heavy and light hole bands, larger effective masses), (iii) generally smaller band offsets, and (iv) interfaces normally less perfect than in heterostructures such as InGaAs/InAlAs. Here, we present the first quantum cascade structures in the SiGe material system that give rise to well-resolved electroluminescence (EL) in the 10-μm range with a narrow linewidth, ~20 meV. Two sample designs are discussed, one optimized for injection of carriers and the other for an efficient radiative recombination process. We show that proper design of the wells can give a quantum efficiency comparable to that of a III-V cascade laser structure.

The valence band diagram of the cascade structure of sample QC-I is shown in Fig. 1A. A so-called "vertical" transition has been chosen [rather than a "diagonal" transition (*7*)], with a principal block consisting of an active quantum well and injector and collector wells. A $Si_{0.68}Ge_{0.32}$ quantum well 40 Å wide (w1, Fig. 1) is situated next to four coupled SiGe quantum wells (w2 to w5), forming a "mini"-superlattice. The main well w1 contains two quasi-bound heavy hole states (HH1 and HH2) separated by ~130 meV, as well as a light hole state at ~60 meV below HH1. The width and Ge content of the four adjacent wells (Fig. 1) are designed such that, for an electric field of ~50 kV/cm, a series of states in the mini-superlattice have a near-overlapping energy with the HH1 state. This allows for an easy tunneling out from this state and into the injector states in the following period. In contrast, there is a minigap for both heavy hole and light hole states around the energy of the HH2 state, which is constructed so that the transport out from this state is quenched, increasing the probability for a radiative transition between the HH1 and HH2 states. In the usual pattern for a cascade structure, this block is repeated 12 times, although a Si layer (1000 Å wide) is inserted after each fourth repeat to limit the total strain.

The growth was realized on high-resistivity Si(100) substrates by means of molecular beam epitaxy, with a relatively low growth temperature (350°C) to avoid strain relaxation and Ge segregation. A buried Si back contact (1 μm thick), the Si insertion layers, and a Si top contact layer (2000 Å) were all doped p-type (acceptor concentration $N_a = 4 \times 10^{18}$, 2×10^{18}, and 4×10^{18} cm^{-3}, respectively), whereas the rest of the structure only contained the background doping (estimated to be $p \leq 5 \times 10^{16}$ cm^{-3}). Despite the lattice mismatch between Si and Ge leading to a considerable strain in the structure, x-ray diffraction (*8*) and transmission electron microscopy (TEM) indicate a coherent strain in the layers, with no apparent threading dislocations or buckling of the interfaces even in the last period (Fig. 1B). Square mesas (420 μm by 420 μm), with Al top and back contacts annealed at 380°C, were fabricated for both samples QC-I and QC-II (see below) using conventional lithographic processes. Outcoupling of the light was achieved through a facet close (≤50 μm) to the mesa, polished at a 45° angle with respect to the plane of the layers. Because of the setback from the surface and the distribution of the cascaded quantum wells over almost 0.5 μm, the coupling is sensitive to both in-plane transverse electrical (TE) and perpendicular-directed transverse magnetic (TM) polarization (*9*).

EL measurements were performed with the sample mounted in a He flow control cryostat, using a Nicolet Fourier transformation infrared spectrometer in step-scan mode (current pulse length ≤5.2 μs, repetition rate 94.8 kHz) and a nitrogen-cooled HgCdTe detector. A typical spectrum, taken at temper-

---

[1]Laboratory for Micro- and Nanotechnology, Paul Scherrer Institut, CH-5232 Villigen, Switzerland. [2]Institute of Physics, University of Neuchâtel, CH-2000 Neuchâtel, Switzerland. [3]Solid State Physics Laboratory, Eidgenössische Technische Hochschule (ETH) Zürich, CH-8093 Zürich, Switzerland.

*These authors contributed equally to this report.
†To whom correspondence should be addressed. E-mail: gabriel.dehlinger@psi.ch; laurent.diehl@psi.ch
‡Present address: L2M-CNRS, 196 ave. Henri Ravera, F-92220 Bagneux, France.

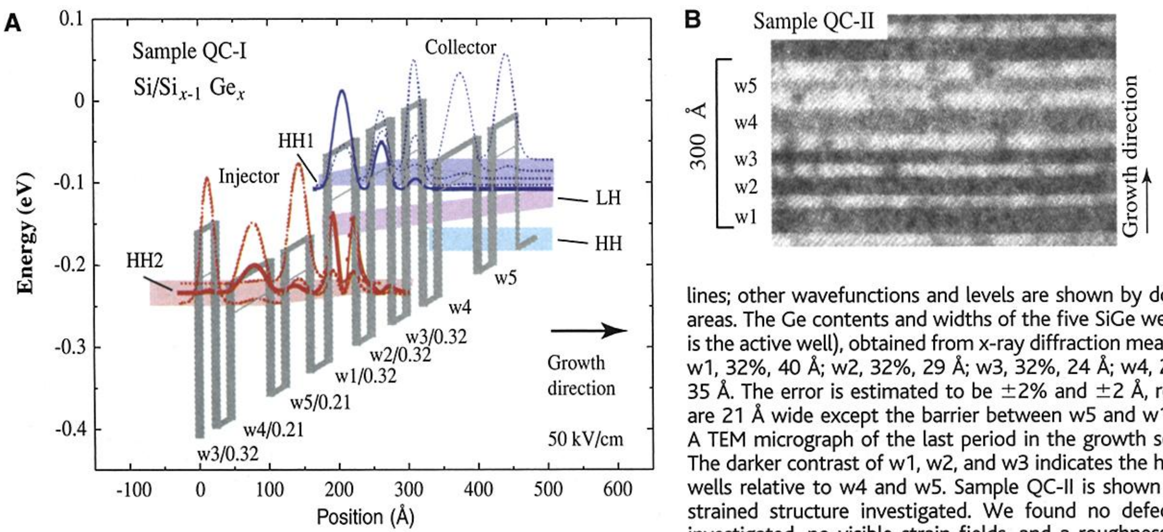

Fig. 1. TEM image and schematics of the samples. (**A**) The valence band potential of sample QC-I for an electric field of 50 kV/cm. The squares of the wavefunctions of the HH1 and HH2 states, between which the transition takes place, are shown by solid lines; other wavefunctions and levels are shown by dotted lines and/or shaded areas. The Ge contents and widths of the five SiGe wells, labeled w1 to w5 (w1 is the active well), obtained from x-ray diffraction measurements, are as follows: w1, 32%, 40 Å; w2, 32%, 29 Å; w3, 32%, 24 Å; w4, 21%, 57 Å; and w5, 21%, 35 Å. The error is estimated to be ±2% and ±2 Å, respectively. All Si barriers are 21 Å wide except the barrier between w5 and w1, which is 26 Å wide. (**B**) A TEM micrograph of the last period in the growth sequence of sample QC-II. The darker contrast of w1, w2, and w3 indicates the higher Ge content in these wells relative to w4 and w5. Sample QC-II is shown because it is the highest strained structure investigated. We found no defects over the whole area investigated, no visible strain fields, and a roughness ≤2 monolayers for the lower interface and ≤3 to 4 monolayers for the upper interface of the wells.

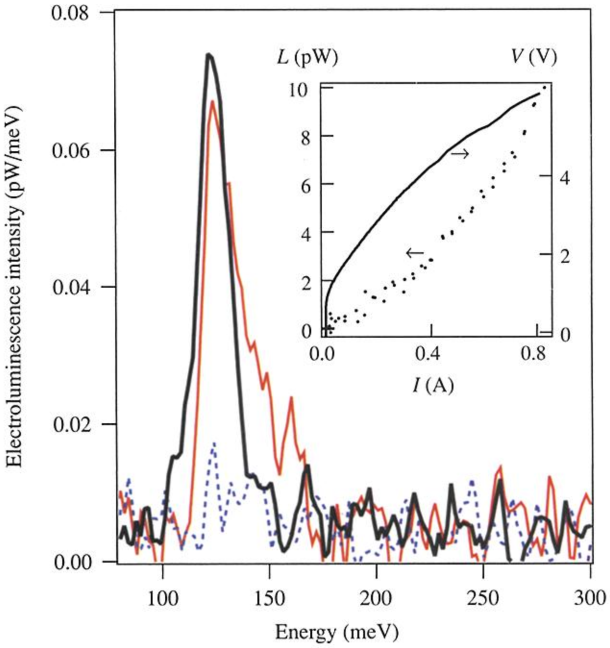

Fig. 2. Electroluminescence spectra of sample QC-I at T = 50 K for I = 250 mA, with 50% duty cycle. The red and dashed blue curves are the TM- and TE-polarized electroluminescence, respectively, at T = 85 K for I = 760 mA, with 50% duty cycle. Inset: Integrated intensity L versus I at T = 85 K (points); and V-I curve at T = 75 K (solid line).

ature $T = 50$ K for a current $I = 250$ mA (corresponding to a bias $V = 3.65$ V), is shown in Fig. 2. The emission energy of ~125 meV is in good agreement with the value of 130 meV expected for the HH2 → HH1 transition. The full width at half maximum (FWHM) of the EL peak, 22 meV, is comparable to the narrowest absorption linewidth reported for Si/SiGe heterostructures (*10*), indicating sharp interfaces and excellent sample quality. The inset in Fig. 2 shows the V-I curve and the integrated EL signal L versus I curve for T around 80 K. (Experimentally, L is measured as the total detector response, letting the signal bypass the Fourier spectrometer.) A current onset is seen at ~1 V. This is even more pronounced at lower temperatures, and can be well explained by the onset of the hole tunneling when the injector states start to align. The L-I relation is reasonably linear, but as the current increases, there is some heating accompanied by a spectral broadening of the luminescence toward higher energies. For these currents, the observed L increases superlinearly with I.

Strong evidence that the luminescence is originating from the intended quantum well transition is given from the polarization of the emitted light (Fig. 2). Because of the weak signal (losses of the polarizer ≈ 2/3), these spectra were measured at higher voltages, 6.0 V (and higher T, 85 K), which is also apparent in the broadening of the peak. As is expected from a HH2 → HH1 transition (*9*, *10*), the light is highly TM polarized.

However, the signal response to the current from sample QC-I is quite weak, indicating a low quantum efficiency, possibly attributable to an insufficient blocking of the tunneling out of holes from the HH2 level. At flat band conditions, this state lies only ~80 meV above the valence band edge, and at high electric fields it is therefore plausible that the holes will be able to tunnel out through the electric field–reduced barrier to continuum states. This effect has been shown to limit the high-T operation of GaAs/AlGaAs QC lasers (*11*).

We used sample QC-II to test the role of escape tunneling. The growth sequence of this sample is similar to that of sample QC-I, but here the levels are better confined as a result of the larger Ge content and width of the active well (41% and 45 Å, respectively). Consequently, the HH2 state lies ~150 meV above the valence band edge at flat band conditions. The Ge contents and widths of the other wells are as follows: w2, 41%, 30 Å; w3, 41%, 27 Å; w4, 21%, 53 Å; and w5, 21%, 31 Å. All Si barriers are 23 Å wide except between the injector and active well (w5 and w1), where it is 26 Å wide. Note that this structure has not been optimized for proper injection into successive active wells, and therefore the current density at moderate bias is rather low.

In the EL spectrum of sample QC-II at 10 K, 9 V bias, and 4 mA (Fig. 3A), the peak energy, 132 meV, is within the errors of the calculated HH2 → HH1 transition at 123 meV. The low current relative to sample QC-I (≈ 1/60 for similar signals), the excellent Lorentzian fit, and the low FWHM of ~20 meV are all noteworthy. The signal shows the same TM polarization as sample QC-I. The emission spectrum taken at 40 mA (Fig. 3A) is stronger by a factor of 2, but the line is also broadened by a factor of ~2, and

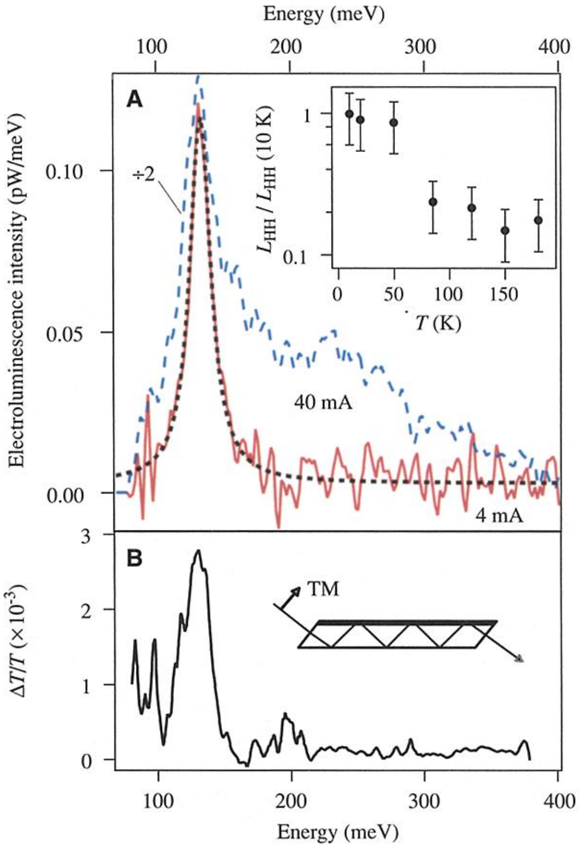

Fig. 3. Electroluminescence and normalized differential absorption of sample QC-II with higher Ge content. **(A)** EL spectra at 10 K for currents of 4 mA (red line) and 40 mA (dashed blue line), using a 50% duty cycle. The dotted line is a Lorentzian fit to the 4-mA curve. Inset: Background corrected integrated intensity of the HH2 → HH1 EL peak, L_{HH} at 40 mA, as a function of T. The values may be overestimated because of the contribution of hot-hole luminescence that cannot be fully separated from the peak. **(B)** Differential absorption ($\Delta T/T$) spectrum between $V = 0$ V and $+1.5$ V, measured with TM-polarized light and at 7 K. Diagram indicates direction of TM polarization.

there is an emergence of a high-energy tail. This contribution probably stems from hot holes being injected into the continuum at high biases, although blackbody radiation associated with carrier or sample heating may also play a role. As expected, this tail has a polarization that is less pronounced than for the main EL peak. Measurements of L (not shown) demonstrate a linear dependence on the current below the onset of the tail, whereas the dependence of the integrated intensity of the main peak around 132 meV is sublinear after the onset. This may be taken as a further indication that, at higher biases, holes tunnel into continuum states rather than into the HH2 state, thus reducing the injection efficiency. The EL decreases at higher temperatures (Fig. 3A, inset) but is still discernible up to 180 K.

The transition energy was also verified by differential absorption spectroscopy (*12*) by modulating the bias voltage between flat band [where most of the carriers are localized in the active well w1 (highest hole energy)] and a small injection bias voltage (where some of the carriers are driven into the adjacent emitter and injector wells w2 to w5). The sharp absorption signal taken at low bias modulation of +1.5 V (Fig. 3B) occurs around 130 meV ($\Delta E_{\mathrm{FWHM}} \approx 22$ meV), in excellent agreement with the expected HH2 → HH1 absorption energy and the observed emission energy. The absorption line at 130 meV is not observed for TE-polarized light. The absolute value of the absorption signal (normalized with respect to the transmission) indicates a voltage modulation of the carrier density on the order of 3.5×10^{10} cm^{-2} per active well.

The low current needed to obtain a discernible signal from sample QC-II is an indication of its higher quantum efficiency, due to better confinement, relative to sample QC-I. The *L-I* curves for both samples are quasi-linear at low currents, which allows us to compare their efficiencies quantitatively. The power is given by

$$P = (1/e) I \eta_{\mathrm{col}} \eta_{\mathrm{QC}} N h\nu \qquad (1)$$

where e is the electron charge, N is the number of quantum cascade periods, η_{col} is the collection efficiency, $h\nu$ is the photon energy, and $\eta_{\mathrm{QC}} = \tau_{\mathrm{nr}}/\tau_{\mathrm{r}}$ is the quantum efficiency per cascade (τ_{nr} and τ_{r} are the nonradiative and radiative lifetimes, respectively). η_{col} was calibrated using an InGaAs/AlInAs quantum cascade light-emitting diode (LED) for which the radiative and nonradiative lifetimes are well established (*13, 14*). A total quantum efficiency $N\eta_{\mathrm{QC}} \approx 10^{-5}$ is obtained for sample QC-II; an efficiency almost two orders of magnitude smaller is obtained for QC-I. The spontaneous radiation lifetime is determined from the dipole moment between the HH1 and HH2 wavefunctions, giving $\tau_{\mathrm{r}} = 0.53$ μs. With this value in Eq. 1, a nonradiative lifetime on the order of 0.5 ps at $T \leq 50$ K is obtained for sample QC-II. As expected from the imperfect cascade alignment, the voltages demanded by QC-II are high (e.g., 13.6 V at 40 mA and 10 K), indicating an inhomogeneous electric field distribution and space-charge buildup. The estimated τ_{nr} should therefore be seen as a lower limit—its value may be as much as four times this estimate for the case of proper injection only into the first block after each Si insertion layer—and thus is comparable to the nonradiative lifetime of III-V vertical transition cascade LEDs (*7*). However, the value is less than theoretical predictions for nonpolar scattering (*6*), although it is similar to that obtained in time-resolved pump-probe experiments for a valence band SiGe quantum well (*15*).

At present, the importance of the light hole state LH1 is unclear. Because of the different pseudo-spin of the light and heavy hole states, optical transitions involving LH1 should in general be weaker than the HH2 → HH1 transition (*10*), but band mixing as well as phonon resonances may increase the light to heavy hole transition rate. Because the detector used here has a cutoff at 80 meV, it has not been possible to study the HH2 → LH1 and LH1 → HH1 transitions.

We have observed well-resolved intersubband EL around 10 μm in Si/SiGe quantum cascade structures. Polarization and absorption measurements clearly show that the signal emanates from the transition between the heavy hole states of the active well (*16*). The radically improved quantum efficiency with improved confinement of the HH2 level gives an indication that a blocking of the tunneling escape in a Si/SiGe cascade structure is possible despite the comparably low band offsets and the presence of both heavy and light hole states in the valence band. Indeed, the lifetimes are comparable to those obtained in III-V cascade LEDs with vertical transitions. This work constitutes a step toward establishing the feasibility of Si/SiGe-based QC lasers. A future challenge is to combine the need for good confinement with good alignment of the cascade levels. A possible path forward is the use of relaxed SiGe buffer layers, which would allow for strain compensation and therefore would yield greater design freedom.

References and Notes

1. J. Faist *et al.*, *Science* **264**, 553 (1994).
2. This does not take into account the momentum transfer to the photon [see, e.g., S. Graf, H. Sigg, K. Köhler, W. Bächthold, *Phys. Rev. Lett.* **84**, 2686 (2000)].
3. R. Q. Yang *et al.*, *Appl. Phys. Lett.* **71**, 2409 (1997).
4. C. Sirtori *et al.*, *Appl. Phys. Lett.* **73**, 3486 (1998).
5. W. Schrenk *et al.*, *Appl. Phys. Lett.* **76**, 253 (1999)
6. G. Sun, L. Friedman, R. A. Soref, *Appl. Phys. Lett.* **66**, 3425 (1995).

7. J. Faist, F. Capasso, C. Sirtori, D. L. Sivco, A. Y. Cho, in *Intersubband Transitions in Quantum Wells, Semiconductor and Semimetal*, H. C. Liu, F. Capasso, Eds. (Academic Press, London, 2000), vol. 66, chap. 1, and references therein.
8. Reciprocal space mapping along the (113) and (224) Bragg planes was performed.
9. T. Fromherz *et al.*, *Appl. Phys. Lett.* **68**, 3611 (1996).
10. T. Fromherz *et al.*, *Phys. Rev. B* **50**, 10573 (1994).
11. P. Kruck *et al.*, *Appl. Phys. Lett.* **76**, 3340 (2000).
12. J. Faist *et al.*, *Appl. Phys. Lett.* **63**, 1354 (1993).
13. J. Faist *et al.*, *Appl. Phys. Lett.* **65**, 94 (1994).
14. S. Blaser *et al.*, unpublished data.
15. P. Boucaud *et al.*, *Appl. Phys. Lett.* **69**, 3069 (1996).
16. In a recent sample we have also been able to demonstrate a confinement shift (observed EL energy, 154 meV; calculated HH2 → HH1 transition, 149 meV).

17. Supported by the Schweizerischer Nationalfonds and Bundesamt für Bildung und Wissenschaft Nr 99 0078. We thank M. Kummer, S. Blaser, D. Hofstetter, and S. Stutz for technical and analytical assistance.

14 September 2000; accepted 15 November 2000

Element-Selective Single Atom Imaging

K. Suenaga,[1,3]* M. Tencé,[1] C. Mory,[1] C. Colliex,[1,2] H. Kato,[4] T. Okazaki,[4] H. Shinohara,[4] K. Hirahara,[3] S. Bandow,[3] S. Iijima[3,5]

Electron energy-loss spectroscopy (EELS) is widely used to identify elemental compositions of materials studied by microscopy. We demonstrate that the sensitivity and spatial resolution of EELS can be extended to the single-atom limit. A chemical map for gadolinium (Gd) clearly reveals the distribution of Gd atoms inside a single chain of metallofullerene molecules (Gd@C$_{82}$) generated within a single-wall carbon nanotube. This characterization technique thus provides the "eyes" to see and identify individual atoms in nanostructures. It is likely to find broad application in nanoscale science and technology research.

Advances in nanotechnology increasingly rely on characterization tools with atomic resolution. Chemical information on heterogeneous nanostructures in particular is more and more crucial for diagnosing and predicting properties of nanodevices. Electron microscopies have long been able to image individual atoms (*1, 2*) but cannot be used to identify elements, because all scattered electrons are collected for imaging. For elemental identification of individual atoms in an electron microscope, only the inelastically scattered electrons that suffer element-specific energy loss must be counted. It has been predicted that the detection limit of EELS should be a single atom (*3*). However, convincing experimental evidence has been lacking because of the absence of fully adapted test objects (*4*).

Here, we demonstrate single-atom spectroscopy by means of EELS. For this purpose, a perfectly suited specimen exhibiting a sequence of individual atoms positioned at regular intervals has been selected. It is found in a recently synthesized hybrid nanomaterial, a single-walled carbon nanotube (SWNT) encapsulating a chain of metallofullerenes (*5*). A scanning transmission electron microscope (VG HB501) that provides a tiny electron beam with a high current flux ($\sim$650 pA in a probe 0.5 to 0.6 nm in diameter) and a high-efficiency charge-coupled device–based detector after an electron spectrometer (modified Gatan PEELS 666) were used for the experiment. The focused incident probe can scan the object under investigation with accurate step increments on the order of angstroms, allowing a whole EELS spectrum to be recorded within a few milliseconds at each probe position. Hence, the intensity of characteristic energy-loss edges can be derived with highly accurate spatial information, and consequently the mapping of the searched element is feasible (*6*).

A chain of endohedral Gd-metallofullerenes was recently generated inside a SWNT by this research group (*5*). Such a material is ideal for demonstrating single-atom spectroscopy, because this structure involves isolated Gd atoms separated by 1 to 2 nm (Fig. 1). The metallofullerene molecules (Gd@C$_{82}$) are aligned within a SWNT. The dark spots seen on each fullerene structure in the high-resolution image are suspected to be the encapsulated Gd atoms (*7*). The interval between the adjacent Gd atoms is large enough with respect to the smallest probe size ($\sim$0.5 nm) accessible with our current electron optics. Element-selective imaging has been performed on a structure similar to that in Fig. 1. A set of 128×32 spectra was recorded with a 3 Å step (consequently, the scanned area corresponds to $\sim 40 \times 10$ nm). Each spectrum was acquired in as little as 35 ms with enough counting statistics. Intensities of the Gd N$_{45}$ edge and carbon K edge were extracted pixel per pixel from all the individual spectra (*8*), and chemical maps for both elements were constructed (Fig. 2).

The bright spots in Fig. 2A are aligned along the nanotube direction, which indicates that they correspond to the Gd atoms. Comparison with the simultaneously obtained carbon map (Fig. 2B) shows that the Gd atoms are located inside the carbon nanotube. This is further confirmed in Fig. 2C, which displays the Gd map (smoothed by convolution with a 3×3 pixel matrix) superposed on the carbon map. Therefore, we can confirm that doping the carbon nanotubes with metallofullerenes has been successful and that the dark spots seen in the high-resolution image (Fig. 1) explicitly correspond to the Gd atoms.

The arrows in Fig. 2B indicate the approximate positions of the individual Gd atoms. The interval between them is about 1 to 3 nm, and some of the Gd atoms are missing. This is probably because the Gd atoms tend to move around from the original positions and, under the intense electron beam, make an aggregate of one to three (or four) atoms associated with a fusion of the adjacent metallofullerenes. Such coalescence processes between the metallofullerenes under the electron beam have also been observed in situ during high-resolution electron microscopy observations. Note that our present spatial resolution ($\sim$0.5 nm) is not sufficient to resolve the carbon layer spacing ($\sim$0.34 nm) between the adjacent fullerenes and nano-

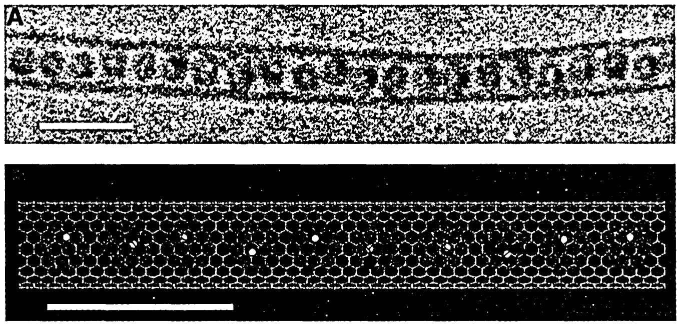

Fig. 1. A conventional high-resolution image (**A**) and a schematic presentation (**B**) of a similar structure. A chain of endohedral Gd-metallofullerenes (Gd@C$_{82}$) is encapsulated in a SWNT. The Gd atoms are shown in yellow in (**B**). Scale bars, 3 nm.

---

[1]Laboratoire de Physique des Solides (CNRS UMR 8502), [2]Laboratoire Aimé Cotton (CNRS UPR 3321), Université Paris-Sud, Orsay 91405, France. [3]Japan Science and Technology Corporation, "Nanotubulites" project, Meijo University, Nagoya 468-8502, Japan. [4]Department of Chemistry, Nagoya University, Nagoya 464-8602, Japan. [5]NEC Corporation, Tsukuba 305-8501, Japan.

*To whom correspondence should be addressed. E-mail: suenaga@meijo-u.ac.jp